

---

# Understanding and Improving Training-free Loss-based Diffusion Guidance

---

Yifei Shen<sup>1\*</sup> Xinyang Jiang<sup>1</sup> Yezhen Wang<sup>2</sup> Yifan Yang<sup>1</sup> Dongqi Han<sup>1</sup> Dongsheng Li<sup>1</sup>  
<sup>1</sup>Microsoft Research Asia <sup>2</sup>National University of Singapore

## Abstract

Adding additional control to pretrained diffusion models has become an increasingly popular research area, with extensive applications in computer vision, reinforcement learning, and AI for science. Recently, several studies have proposed training-free loss-based guidance by using off-the-shelf networks pretrained on clean images. This approach enables zero-shot conditional generation for universal control formats, which appears to offer a free lunch in diffusion guidance. In this paper, we aim to develop a deeper understanding of training-free guidance, as well as overcome its limitations. We offer a theoretical analysis that supports training-free guidance from the perspective of optimization, distinguishing it from classifier-based (or classifier-free) guidance. To elucidate their drawbacks, we theoretically demonstrate that training-free guidance is more susceptible to adversarial gradients and exhibits slower convergence rates compared to classifier guidance. We then introduce a collection of techniques designed to overcome the limitations, accompanied by theoretical rationale and empirical evidence. Our experiments in image and motion generation confirm the efficacy of these techniques.

## 1 Introduction

Diffusion models represent a class of powerful deep generative models that have recently broken the long-standing dominance of generative adversarial networks (GANs) [8]. These models have demonstrated remarkable success in a variety of domains, including the generation of images and videos in computer vision [31, 3], the synthesis of molecules and proteins in computational biology [18, 49], as well as the creation of trajectories and actions in the field of reinforcement learning (RL) [19].

One critical area of research in the field of diffusion models involves enhancing controllability, such as pose manipulation in image diffusion [47], modulation of quantum properties in molecule diffusion [18], and direction of goal-oriented actions in RL diffusion [21]. The predominant techniques for exerting control over diffusion models include classifier guidance and classifier-free guidance. Classifier guidance involves training a time-dependent classifier to map a noisy image, denoted as  $x_t$ , to a specific condition  $y$ , and then employing the classifier’s gradient to influence each step of the diffusion process [8]. Conversely, classifier-free guidance bypasses the need for a classifier by training an additional diffusion model conditioned on  $y$  [16]. However, both approaches necessitate extra training to integrate the conditions. Moreover, their efficacy is often constrained when the data-condition pairs are limited and typically lack the capability for zero-shot generalization to novel conditions.

Recently, several studies [2, 46, 35] have introduced training-free guidance that builds upon the concept of classifier guidance. These models eschew the need for training a classifier on noisy images; instead, they estimate the clean image from its noisy counterpart using Tweedie’s formula and then

---

\*yifeishen@microsoft.com

employ pre-trained networks, designed for clean images, to guide the diffusion process. Given that checkpoints for these networks pretrained on clean images are widely accessible online, this form of guidance can be executed in a zero-shot manner. A unique advantage of training-free guidance is that it can be applied to universal control formats, such as style, layout, and FaceID [2, 46, 35] without any additional training efforts. Furthermore, these algorithms have been successfully applied to offline reinforcement learning, enabling agents to achieve novel goals not previously encountered during training [42]. In contrast to classifier guidance and classifier-free guidance, it is proved in [25] that training-free guidance does not offer an approximation to the exact conditional energy. Therefore, from a theoretical perspective, it is intriguing to understand how and when these methods succeed or fail. From an empirical standpoint, it is crucial to develop algorithms that can address and overcome these limitations.

This paper seeks to deepen the understanding of training-free guidance by examining its mechanisms and inherent limitations, as well as overcoming these limitations. Specifically, our major contributions can be summarized as follows:

- **How does training-free guidance work?** Although exact conditional energy is difficult to approximate in a training-free manner, from the optimization standpoint, we show that training-free guidance can effectively decrease the guidance loss function. The optimization perspective clarifies the mystery of why the guidance weights should be meticulously designed in relation to the guidance function and diffusion time, as observed in [46].
- **When does training-free guidance not work?** We theoretically identify the susceptibility of training-free guidance to adversarial gradient issues and slower convergence rates. We attribute these challenges to a decrease in the smoothness of the guidance network in contrast to the classifier guidance.
- **Improving training-free guidance:** We introduce random augmentation to alleviate the adversarial gradient and Polyak step size scheduling to improve convergence. The efficacy of these methods is empirically confirmed across various diffusion models (i.e., image diffusion and motion diffusion) and under multiple conditions (i.e., segmentation, sketch, text, object avoidance, and targeting)<sup>2</sup>.

## 2 Preliminaries

### 2.1 Diffusion Models

Diffusion models are characterized by forward and reverse processes. The forward process, occurring over a time interval from 0 to  $T$ , incrementally transforms an image into Gaussian noise. On the contrary, the reverse process, from  $T$  back to 0, reconstructs the image from the noise. Let  $\mathbf{x}_t$  represent the state of the data point at time  $t$ ; the forward process systematically introduces noise to the data by following a predefined noise schedule given by  $\mathbf{x}_t = \sqrt{\alpha_t}\mathbf{x}_0 + \sigma_t\boldsymbol{\epsilon}_t$ , where  $\alpha_t \in [0, 1]$  is monotonically decreasing with  $t$ ,  $\sigma_t = \sqrt{1 - \alpha_t}$ , and  $\boldsymbol{\epsilon}_t \sim \mathcal{N}(0, \mathbf{I})$  is random noise. Diffusion models use a neural network to learn the noise at each step:

$$\min_{\theta} \mathbb{E}_{\mathbf{x}_t, \boldsymbol{\epsilon}_t} [\|\boldsymbol{\epsilon}_{\theta}(\mathbf{x}_t, t) - \boldsymbol{\epsilon}_t\|_2^2] = \min_{\theta} \mathbb{E}_{\mathbf{x}_t, \boldsymbol{\epsilon}_t} [\|\boldsymbol{\epsilon}_{\theta}(\mathbf{x}_t, t) + \sigma_t \nabla_{\mathbf{x}_t} \log p_t(\mathbf{x}_t)\|_2^2],$$

where  $p_t(\mathbf{x}_t)$  is the distribution of  $\mathbf{x}_t$ . The reverse process is obtained by the following ODE:

$$\frac{d\mathbf{x}_t}{dt} = f(t)\mathbf{x}_t - \frac{g^2(t)}{2} \nabla_{\mathbf{x}_t} \log p_t(\mathbf{x}_t) = f(t)\mathbf{x}_t + \frac{g^2(t)}{2\sigma_t} \boldsymbol{\epsilon}_{\theta}(\mathbf{x}_t, t), \quad (1)$$

where  $f(t) = \frac{d \log \sqrt{\alpha_t}}{dt}$ ,  $g^2(t) = \frac{d\sigma_t^2}{dt} - 2 \frac{d \log \sqrt{\alpha_t}}{dt} \sigma_t^2$ . The reverse process enables generation as it converts a Gaussian noise into the image.

### 2.2 Diffusion Guidance

In diffusion control, we aim to sample  $\mathbf{x}_0$  given a condition  $\mathbf{y}$ . The conditional score function is expressed as follows:

$$\nabla_{\mathbf{x}_t} \log p_t(\mathbf{x}_t|\mathbf{y}) = \nabla_{\mathbf{x}_t} \log p_t(\mathbf{x}_t) + \nabla_{\mathbf{x}_t} \log p_t(\mathbf{y}|\mathbf{x}_t). \quad (2)$$

<sup>2</sup>The code is available at <https://github.com/BIGknight/Understanding-Training-free-Diffusion-Guidance>

The conditions are specified by the output of a neural network, and the energy is quantified by the corresponding loss function. If  $\ell(f_\phi(\cdot), \cdot)$  represents the loss function as computed by neural networks, then the distribution of the clean data is expected to follow the following formula [2, 46, 35]:

$$p_0(\mathbf{x}_0|\mathbf{y}) \propto p_0(\mathbf{x}_0) \exp(-\ell(f_\phi(\mathbf{x}_0), \mathbf{y})). \quad (3)$$

For instance, consider a scenario where the condition is the object location. In this case,  $f_\phi$  represents a fastRCNN architecture, and  $\ell$  denotes the classification loss and bounding box loss. By following the computations outlined in [25], we can derive the exact formula for the second term in the RHS of (2) as:

$$\nabla_{\mathbf{x}_t} \log p_t(\mathbf{y}|\mathbf{x}_t) = \nabla_{\mathbf{x}_t} \log \mathbb{E}_{p(\mathbf{x}_0|\mathbf{x}_t)} [\exp(-\ell(f_\phi(\mathbf{x}_0), \mathbf{y}))]. \quad (4)$$

**Classifier guidance** [8] involves initially training a time-dependent classifier to predict the output of the clean image  $\mathbf{x}_0$  based on noisy intermediate representations  $\mathbf{x}_t$  during the diffusion process, i.e., to train a time-dependent classifier  $f_\psi(\mathbf{x}_t, t)$  such that  $f_\psi(\mathbf{x}_t, t) \approx f_\phi(\mathbf{x}_0)$ . Then the gradient of the time-dependent classifier is used for guidance, given by  $\nabla_{\mathbf{x}_t} \log p_t(\mathbf{y}|\mathbf{x}_t) := -\nabla_{\mathbf{x}_t} \ell(f_\psi(\mathbf{x}_t, t), \mathbf{y})$ .

**Training-free loss-based guidance** [2, 46, 6] puts the expectation in (4) inside the loss function:

$$\nabla_{\mathbf{x}_t} \log p_t(\mathbf{y}|\mathbf{x}_t) := \nabla_{\mathbf{x}_t} \log [\exp(-\ell(f_\phi(\mathbb{E}_{p(\mathbf{x}_0|\mathbf{x}_t)}(\mathbf{x}_0)), \mathbf{y}))] \stackrel{(a)}{=} -\nabla_{\mathbf{x}_t} \ell \left[ f_\phi \left( \frac{\mathbf{x}_t - \sigma_t \epsilon_\theta(\mathbf{x}_t, t)}{\sqrt{\alpha_t}} \right), \mathbf{y} \right], \quad (5)$$

where (a) uses Tweedie’s formula  $\mathbb{E}_{p(\mathbf{x}_0|\mathbf{x}_t)}(\mathbf{x}_0) = \frac{\mathbf{x}_t - \sigma_t \epsilon_\theta(\mathbf{x}_t, t)}{\sqrt{\alpha_t}}$ . Leveraging this formula permits the use of a pre-trained off-the-shelf network designed for processing clean data. The gradient of the last term in the energy function is obtained via backpropagation through both the guidance network and the diffusion backbone.

### 3 Analysis of Training-Free Guidance

#### 3.1 How does Training-free Guidance Work?

**On the difficulty of approximating  $\nabla_{\mathbf{x}_t} \log p_t(\mathbf{y}|\mathbf{x}_t)$  in high-dimensional space.** Despite its intuitive, [25] has shown that training-free guidance in (5) does not offer an approximation to the true energy in (4). The authors of [35] considers to directly approximate (4) with Gaussian distribution:

$$\begin{aligned} \nabla_{\mathbf{x}_t} \log \mathbb{E}_{p(\mathbf{x}_0|\mathbf{x}_t)} [\exp(-\ell(f_\phi(\mathbf{x}_0), \mathbf{y}))] &\stackrel{(a)}{\approx} \nabla_{\mathbf{x}_t} \log \mathbb{E}_{q(\mathbf{x}_0|\mathbf{x}_t)} [\exp(-\ell(f_\phi(\mathbf{x}_0), \mathbf{y}))] \\ &\approx \nabla_{\mathbf{x}_t} \log \frac{1}{n} \sum_{i=1}^n \exp(-\ell(f_\phi(\mathbf{x}_0^i), \mathbf{y})), \quad \mathbf{x}_0^i \sim q(\mathbf{x}_0|\mathbf{x}_t), \end{aligned} \quad (6)$$

where  $q(\mathbf{x}_0|\mathbf{x}_t)$  is chosen as  $\mathcal{N}(\mathbb{E}_{p(\mathbf{x}_0|\mathbf{x}_t)}(\mathbf{x}_0), r_t^2 \mathbf{I})$  and  $r_t$  is a tunable parameter. As demonstrated in [35], the approximation is effective for one-dimensional distribution. However, we find that the approximation denoted by (a) does not extend to high-dimensional data (e.g., images) if the surrogate distribution  $q$  is sub-Gaussian. This is due to the well-known high-dimensional probability phenomenon [41] that if  $q$  has sub-Gaussian coordinates (e.g., iid and bounded), then  $q(\mathbf{x}_0|\mathbf{x}_t)$  tends to concentrate on a spherical shell centered at  $\mathbb{E}_{p(\mathbf{x}_0|\mathbf{x}_t)}(\mathbf{x}_0)$  with radius  $r_t$  (details are in Appendix C.1). Since the spherical shell represents a low-dimensional manifold with zero measure in the high-dimensional space, there is a significant likelihood that the supports of  $p(\mathbf{x}_0|\mathbf{x}_t)$  and  $q(\mathbf{x}_0|\mathbf{x}_t)$  do not overlap, rendering the approximation (a) ineffective.

**Understanding training-free guidance from an optimization perspective.** We instead analyze the training-free guidance from the optimization perspective. Intuitively, in each step, the gradient is taken and the objective function decreases. At the initial stage of the diffusion ( $t$  is large), the diffusion trajectory can exhibit substantial deviations between adjacent steps and may increase the objective value. So the objective value will oscillate at the beginning. When  $t$  is smaller, the change to the sample is more fine-grained, leading to a bounded change in the objective value. Therefore, the objective value is guaranteed to decrease when  $t$  is small, as showing in the next proposition.

**Proposition 3.1.** *Assume that the guidance loss function  $\ell(f_\phi(\mathbf{x}_0), \mathbf{y})$  is  $\mu$ -PL (defined in Definition D.2 in appendix) and  $L_f$ -Lipschitz with respect to clean images  $\mathbf{x}_0$ , and the score function  $\nabla \log p_t(\mathbf{x}_t)$  is  $L_p$ -Lipschitz (defined in Definition D.1 in appendix) with respect to noisy image  $\mathbf{x}_t$ .*

Denote  $\lambda_{\min}$  as the minimum eigenvalue of the (semi)-definite matrix  $\text{Cov}[\mathbf{x}_0|\mathbf{x}_t]$ . Then the following conditions hold: (1) Consider the loss function  $\ell_t(\mathbf{x}_t) = \ell\left(f_\phi\left(\frac{\mathbf{x}_t + \sigma_t^2 \nabla \log p_t(\mathbf{x}_t)}{\sqrt{\alpha_t}}\right), \mathbf{y}\right)$  and denote  $\kappa_1 = \frac{\mu \lambda_{\min}^2}{L_f(1+L_p)\sqrt{\alpha_t}\sigma_t^4}$ . After one gradient step  $\hat{\mathbf{x}}_t = \mathbf{x}_t - \eta \nabla_{\mathbf{x}_t} \ell_t(\mathbf{x}_t)$ ,  $\eta = \frac{\sqrt{\alpha_t}}{L_f(1+L_p)}$ , we have  $\ell_t(\hat{\mathbf{x}}_t) \leq (1 - \kappa_1)\ell_t(\mathbf{x}_t)$ ; (2) Consider a diffusion process that adheres to a bounded change in the objective function such that for any diffusion step, i.e.,  $\ell_{t-1}(\mathbf{x}_{t-1}) \leq \frac{\ell_t(\hat{\mathbf{x}}_t)}{(1-\kappa_2)}$  for some  $\kappa_2 < \kappa_1$ , then the objective function converges at a linear rate, i.e.,  $\ell_{t-1}(\mathbf{x}_{t-1}) \leq \frac{1-\kappa_1}{1-\kappa_2}\ell_t(\mathbf{x}_t)$ .

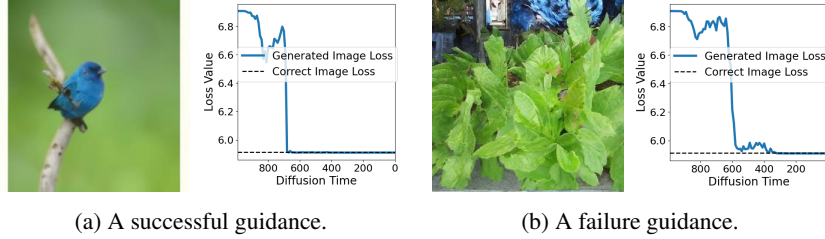


Figure 1: The classifier loss of a successful and a failure guidance example. The target class is “indigo bird”.

The proof is given in Appendix D.2. The Lipschitz continuity and PL conditions are basic assumptions in optimization, and it has been shown that neural networks can locally satisfy these conditions [5]. In Figure 1, we use ResNet-50 trained on clean images to guide ImageNet pre-trained diffusion models. The loss value at each diffusion step is plotted. As a reference, we choose 100 images from the class “indigo bird” in ImageNet training set and compute the loss value, which is referred as “Correct Image Loss” in the figure. The objective value oscillates when  $t$  is large, followed by a swift decrease, which verifies our analysis. Furthermore, the optimization perspective resolves the mystery of why the guidance weights (i.e., the step size in optimization) should be carefully selected with respect to the guidance function and time  $t$  [46]. In [46], most guidance weights  $\eta$  are chosen to be proportional to  $\sqrt{\alpha_t}$  and dependent on guidance network, which differs from the weights used in classifier guidance and precisely aligns with our findings in Proposition 3.1. Remarkably, from theory and experiments, we see that training-free guidance can achieve low loss levels even in instances of guidance failure (Figure 1b). This is attributed to the influence of adversarial gradients, as discussed in the next subsection.

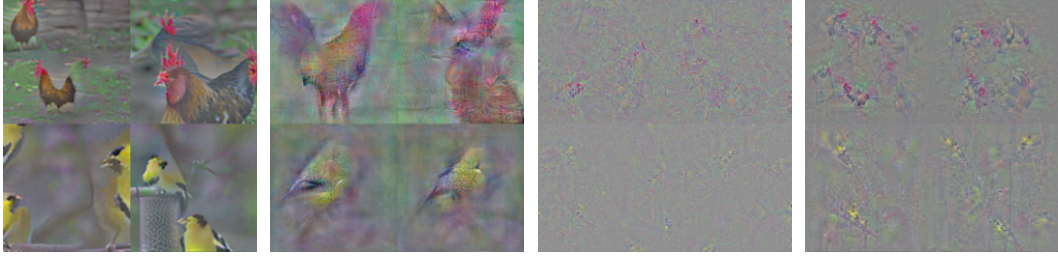
### 3.2 Limitations of Training-free Guidance

In this subsection, we examine the disadvantages of employing training-free guidance networks as opposed to training-based classifier guidance.

**Training-free guidance is more sensitive to the adversarial gradient.** Adversarial gradient is a significant challenge for neural networks, which refers to minimal perturbations deliberately applied to inputs that can induce disproportionate alterations in the model’s output [36]. The resilience of a model to adversarial gradients is often analyzed through the lens of its Lipschitz constant [32]. If the model has a lower Lipschitz constant, then the output is less sensitive to the input perturbations and thus is more robust. In classifier guidance, time-dependent classifiers are trained on noise-augmented images. Our finding is that adding Gaussian noise transforms non-Lipschitz classifiers into Lipschitz ones. This transition mitigates the adversarial gradient challenge by inherently enhancing the model’s robustness to such perturbations, as shown in the next proposition.

**Proposition 3.2.** (Time-dependent network is more robust and smooth) Given a bounded non-Lipschitz loss function  $\ell(\mathbf{x}) \leq C$ , the loss  $\hat{\ell}(\mathbf{x}) = \mathbb{E}_{\epsilon \sim \mathcal{N}(0, I)}[\ell(\mathbf{x} + \sigma_t \epsilon)]$  is  $C\sqrt{\frac{2}{\pi\sigma_t^2}}$ -Lipschitz and  $\nabla \hat{\ell}$  is  $\frac{2C}{\sigma_t}$ -Lipschitz.

The proof is given in Appendix D.3. We present visualizations of the accumulated gradients for both the time-dependent and off-the-shelf time-independent classifiers corresponding to different classes in Figure 2b and Figure 2c, respectively. These visualizations are generated by initializing an image with a random background and computing 1000 gradient steps for each classifier. For the time-dependent



(a) Adversarially robust classifier. (b) Time-dependent classifier. (c) Off-the-shelf ResNet-50 classifier. (d) ResNet-50 with random augmentation.

Figure 2: Gradients of different classifiers on random backgrounds. The images in the first row correspond to the target class “cock”, and the second row to “goldfinch”.

classifier, the input time for the  $t$ -th gradient step is  $1000 - t$ . The images are generated purely by the classifier gradients without diffusion involved. For comparative analysis, we include the accumulated gradient of an adversarially robust classifier [33], as shown in Figure 2a, which has been specifically trained to resist adversarial gradients. The resulting plots reveal a stark contrast: the gradient of the time-dependent classifier visually resembles the target image, whereas the gradient of the time-independent classifier does not exhibit such recognizability. This observation suggests that off-the-shelf time-independent classifiers are prone to generating adversarial gradients compared to the time-dependent classifier used in classifier guidance. In contrast to yielding a direction that meaningfully minimizes the loss, the adversarial gradient primarily serves to minimize the loss in a manner that is not necessarily aligned with the intended guidance direction.

**Training-free guidance slows down the convergence of reverse ODE.** The efficiency of an algorithm in solving reverse ordinary differential equations is often gauged by the number of non-linear function estimations (NFEs) required to achieve convergence. This metric is vital for algorithmic design, as it directly relates to computational cost and time efficiency [34]. In light of this, we explore the convergence rates associated with various guidance paradigms, beginning our analysis with a reverse ODE framework that incorporates a generic gradient guidance term. The formula is expressed as

$$\frac{d\mathbf{x}_t}{dt} = f(t)\mathbf{x}_t + \frac{g^2(t)}{2}(\epsilon_\theta(\mathbf{x}_t, t) + \nabla_{\mathbf{x}_t} h(\mathbf{x}_t, t)), \quad (7)$$

where  $h(\cdot, \cdot)$  can be either a time-dependent classifier or a time-independent classifier with Tweedie’s formula. The subsequent proposition elucidates the relationship between the discretization error and the smoothness of the guidance function.

**Proposition 3.3.** *Let  $g(\mathbf{x}_t, t) = \epsilon_\theta(\mathbf{x}_t, t) + \nabla_{\mathbf{x}_t} h(\mathbf{x}_t, t)$  in (7). Assume that  $g(\mathbf{x}_t, t)$  is  $L$ -Lipschitz. Then the discretization error of the DDIM solver is bounded by  $O(h_{\max} + Lh_{\max})$ , where  $h_{\max} = \max_t \frac{1}{2} \left[ \log\left(\frac{\alpha_t}{1-\alpha_t}\right) - \log\left(\frac{\alpha_{t-1}}{1-\alpha_{t-1}}\right) \right]$ .*

The proof is given in Appendix D.4. Proposition 3.2 establishes that time-dependent classifiers exhibit superior gradient Lipschitz constants compared to their off-the-shelf time-independent counterparts. This disparity in smoothness slows down the convergence for training-free guidance methods, necessitating a greater number of NFEs to achieve the desired level of accuracy when compared to classifier guidance.

## 4 Improving Training-free Guidance

In this section, we propose to adopt random augmentation to mitigate the adversarial gradient issue, and Polyak step size to mitigate the convergence issue. Time travel was adopted in previous studies [2, 46, 14] without theoretical justifications. We theoretically analyze this trick in Appendix C.2, which completes the picture for the tricks to improve training-free guidance.

---

**Algorithm 1** Random Augmentation

---

```

for  $t = T, \dots, 0$  do
   $\mathbf{x}_{t-1} = \text{DDIM}(\mathbf{x}_t)$ 
   $\hat{\mathbf{x}}_0 = \frac{\mathbf{x}_t - \sigma_t \epsilon_\theta(\mathbf{x}_t, t)}{\sqrt{\alpha_t}}$ 
   $\mathbf{g}_t = \frac{1}{|\mathcal{T}|} \sum_{T \in \mathcal{T}} \nabla_{\mathbf{x}_t} \ell(f_\phi(T(\hat{\mathbf{x}}_0)), \mathbf{y})$ 
   $\mathbf{x}_{t-1} = \mathbf{x}_{t-1} - \eta \cdot \mathbf{g}_t$ 
end for

```

---



---

**Algorithm 2** Polyak Step Size

---

```

for  $t = T, \dots, 0$  do
   $\mathbf{x}_{t-1} = \text{DDIM}(\mathbf{x}_t)$ 
   $\hat{\mathbf{x}}_0 = \frac{\mathbf{x}_t - \sigma_t \epsilon_\theta(\mathbf{x}_t, t)}{\sqrt{\alpha_t}}$ 
   $\mathbf{g}_t = \nabla_{\mathbf{x}_t} \ell(f_\phi(\hat{\mathbf{x}}_0), \mathbf{y})$ 
   $\mathbf{x}_{t-1} = \mathbf{x}_{t-1} - \eta \cdot \frac{\|\epsilon_\theta(\mathbf{x}_t, t)\|}{\|\mathbf{g}_t\|_2} \cdot \mathbf{g}_t$ 
end for

```

---

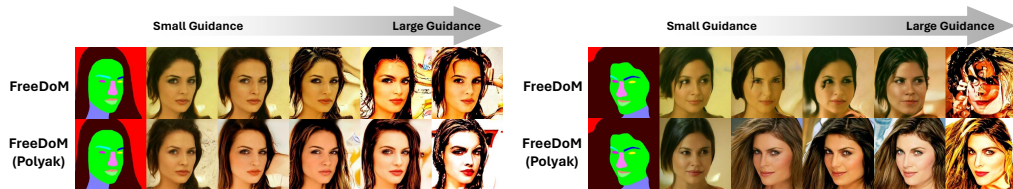
## 4.1 Random Augmentation

As established by Proposition 3.2, the introduction of Gaussian perturbations enhances the Lipschitz property of a neural network. A direct application of this principle involves creating multiple noisy instances of an estimated clean image and incorporating them into the guidance network, a method analogous to the one described in (6). However, given the high-dimensional nature of image data, achieving a satisfactory approximation of the expected value necessitates an impractically large number of noisy copies. To circumvent this issue, we propose an alternative strategy that employs a diverse set of data augmentations in place of solely adding Gaussian noise. This approach effectively introduces perturbations within a lower-dimensional latent space, thus requiring fewer samples. The suite of data augmentations utilized, denoted by  $\mathcal{T}$ , is derived from the differentiable data augmentation techniques outlined in [48], which encompasses transformations such as translation, resizing, color adjustments, and cutout operations. The details are shown in Algorithm 1 and the rationale is shown in the following proposition.

**Proposition 4.1.** (Random augmentation improves smoothness) *Given a bounded non-Lipschitz loss function  $\ell(\mathbf{x})$ , the loss  $\hat{\ell}(\mathbf{x}) = \mathbb{E}_{\epsilon \sim p(\epsilon)}[\ell(\mathbf{x} + \epsilon)]$  is  $C \int_{\mathbb{R}^n} \|\nabla p(\mathbf{t})\|_2 d\mathbf{t}$ -Lipschitz and its gradient is  $C \int_{\mathbb{R}^n} \|\nabla^2 p(\mathbf{t})\|_{op} d\mathbf{t}$ -Lipschitz.*

The proof is shown in Appendix D.5. Echoing the experimental methodology delineated in Section 3.2, we present an analysis of the accumulated gradient effects when applying random augmentation to a ResNet-50 model. Specifically, we utilize a set of  $|\mathcal{T}| = 10$  diverse transformations as our augmentation strategy. The results of this experiment are visualized in Figure 2d, where the target object’s color and shape emerges in the gradient profile. This observation suggests that the implementation of random augmentation can alleviate the adversarial gradient issue. The efficiency of random augmentation is further discussed in Appendix C.3.

## 4.2 Polyak Step Size



(a) When the initialization is proximate to the specified conditions, both step sizes perform satisfactorily. (b) When the initialization deviates from the conditions, only the Polyak step size guides effectively.

Figure 3: The effects of step size.

In Section 3.1, we analyzed training-free guidance from the optimization perspective. To accelerate the convergence, gradient step size should be adaptive to the gradient landscape. We adopt Polyak step size, which has near-optimal convergence rates under various conditions [13]. The algorithm is shown in Algorithm 2 and the term  $\|\epsilon_\theta(\mathbf{x}_t, t)\|$  is used to both estimate the gap to optimal values and balance the magnitude of diffusion term and guidance term.

We implement Polyak step size within the context of a training-free guidance framework called FreeDoM [46] and benchmark the performance of this implementation using the DDIM sampler

Methods	Segmentation maps		Sketches		Texts	
	Distance↓	FID↓	Distance↓	FID↓	Distance↓	FID↓
UG [2]	2247.2	39.91	52.15	47.20	12.08	44.27
LGD-MC [35]	2088.5	38.99	49.46	54.47	11.84	41.74
FreeDoM [46]	1657.0	38.65	34.21	52.18	11.17	46.13
MPGD-Z [14]	1976.0	39.81	37.23	54.18	10.78	42.45
Ours	<b>1575.7</b>	<b>33.31</b>	<b>30.41</b>	<b>41.26</b>	<b>10.72</b>	<b>41.25</b>

Table 1: The performance comparison of various methods on CelebA-HQ with different types of zero-shot guidance. The experimental settings adhere to Table 1 of [46].

Methods	LGD-MC [35]	UG [2]	FreeDoM [46]	MPGD-Z [14]	Ours
CLIP Score↑	24.3	25.7	25.9	25.1	<b>27.7</b>

Table 2: The performance comparison of various methods on unconditional ImageNet with zero-shot text guidance. We compare various methods using ImageNet pre-trained diffusion models with CLIP-B/16 guidance. For evaluating performance, the CLIP score is computed using CLIP-L/14.

with 50 steps. As shown in Figure 3, FreeDoM is unable to effectively guide the generation process when faced with a significant discrepancy between the unconditional generation and the specified condition. An illustrative example is the difficulty in guiding the model to generate faces oriented to the left when the unconditionally generated faces predominantly orient to the right, as shown in Figure 3b. This challenge, which arises due to the insufficiency of 50 steps for convergence under the condition, is ameliorated by substituting gradient descent with adaptive step size, thereby illustrating the benefits of employing a better step size in the guidance process.

## 5 Experiments

In this section, we evaluate the efficacy of our proposed techniques across various diffusion models and guidance conditions. We compare our methods with established baselines: Universal Guidance (UG) [2], Loss-Guided Diffusion with Monte Carlo (LGD-MC) [35], Training-Free Energy-Guided Diffusion Models (FreeDoM) [46], and Manifold Preserving Guided Diffusion (MPGD) [14]. LGD-MC utilizes (6) while UG and FreeDoM are built on (5). MPGD utilizes an auto-encoder to ensure the manifold constraints. Furthermore, time travel trick (Algorithm 3) is adopted in UG, FreeDoM, and MPGD to improve the performance. Please refer to Appendix B for details. For the sampling method, DDIM with 100 steps is adopted as in [46, 35]. The method ‘‘Ours’’ is built on FreeDoM, with Polyak step size and random augmentation.

### 5.1 Guidance to CelebA-HQ Diffusion

In this subsection, we adopt the experimental setup from [46]. Specifically, we utilize the CelebA-HQ diffusion model [17] to generate high-quality facial images. We explore three guidance conditions: segmentation, sketch, and text. For segmentation guidance, BiSeNet [45] generates the facial segmentation maps, with an  $\ell_2$ -loss applied between the estimated map of the synthesized image and the provided map. Sketch guidance involves using the method from [43] to produce facial sketches, where the loss function is the  $\ell_2$ -loss between the estimated sketch of  $\hat{x}_0$  and the given sketch. For text guidance, we employ CLIP [30] as both the image and text encoders, setting the loss to be the  $\ell_2$  distance between the image and text embeddings.

We randomly select 1000 samples each of segmentation maps, sketches, and text descriptions. The comparative results are presented in Table 1. Consistent with [46], the time-travel number for all methods is set to  $s = 1$ . Figure 4 displays a random selection of the generated images. More image samples are provided in the supplementary materials. We find that the baselines failed to guide if the condition differs from unconditionally generated images significantly, as discussed in Section 4.2.

### 5.2 Guidance to ImageNet Diffusion

For the unconditional ImageNet diffusion, we employ text guidance in line with the approach used in FreeDoM and UG [2, 46]. We utilize CLIP-B/16 as the image and text encoder, with cosine similarity serving as the loss function to measure the congruence between the image and text embeddings.

Methods	“Backwards”		“Balanced Beam”		“Walking”		“Jogging”	
	Loss↓	CLIP↑	Loss↓	CLIP↑	Loss↓	CLIP↑	Loss↓	CLIP↑
Unconditional [38]	3.55 + 9.66	65.6	47.92 + 0	<b>70.8</b>	48.88 + 0	37.6	144.84 + 0	<b>61.72</b>
FreeDoM [46]	1.09 + 6.63	67.23	9.83 + 4.48	62.65	1.64 + 7.55	40.12	34.95 + 7.83	58.74
LGD-MC [35]	0.98 + 6.48	67.31	4.42 + 0.02	63.13	1.30 + 0.39	38.82	6.12 + 2.38	57.89
Ours	<b>0.68+1.32</b>	<b>67.50</b>	<b>1.13+0.30</b>	63.02	<b>0.43+0.31</b>	<b>40.40</b>	<b>2.93+1.15</b>	60.03

Table 3: Comparison of various methods on MDM with zero-shot targeting and object avoidance guidance. Loss is reported as a two-component metric: the first part is the MSE between the target and the actual final position of the individual; the second part measures the object avoidance loss.

To evaluate performance and mitigate the potential for high-scoring adversarial images, we use CLIP-L/14 for computing the CLIP score. In FreeDoM and MPGD-Z, resampling is conducted for time steps ranging from 800 to 300, with the time-travel number fixed at 10, as described in [46]. Given that UG resamples at every step, we adjust its time-travel number  $s = 5$  to align the execution time with that of FreeDoM. The textual prompts for our experiments are sourced from [23]. The comparison of different methods is depicted in Table 2. The corresponding randomly selected images are illustrated in Figure 5. The table indicates that our method achieves the highest consistency with the provided prompts. As shown in Figure 5, LGD-MC and MPGD tend to overlook elements of the prompts. Both UG and FreeDoM occasionally produce poorly shaped objects, likely influenced by adversarial gradients. Our approach addresses this issue through the implementation of random augmentation. Additionally, none of the methods successfully generate images that accurately adhere to positional prompts such as “left to” or “below”. This limitation is inherent to CLIP and extends to all text-to-image generative models [39]. More image samples are provided in the supplementary materials.

### 5.3 Guidance to Human Motion Diffusion

In this subsection, we extend our evaluation to human motion generation using the Motion Diffusion Model (MDM) [38], which represents motion through a sequence of joint coordinates and is trained on a large corpus of text-motion pairs with classifier-free guidance. We apply the targeting guidance and object avoidance guidance as described in [35]. Let  $\mathbf{x}_0(t)$  denote the joint coordinates at time  $t$ ,  $\mathbf{y}_t$  the target location,  $\mathbf{y}_{\text{obs}}$  the obstacle location,  $r$  the radius of the objects, and  $T$  the total number of frames. The loss function is defined as follows:

$$\ell = \|\mathbf{y}_t - \mathbf{x}_0(T)\|_2^2 + \sum_i \text{sigmoid}(-(\|\mathbf{x}_0(i) - \mathbf{y}_{\text{obs}}\| - r) \times 50) \times 100. \quad (8)$$

Our experimental configuration adheres to the guidelines set forth in [35]. We assess the methods using the targeting loss (the first term in (8)), the object avoidance loss (the second term in (8)), and the CLIP score calculated by MotionCLIP [37]. In this application, MPGD-Z cannot be applied as there are no auto-encoder. MPGD w/o proj suffers from the shortcut and cannot achieve good performance, as discussed in Appendix B.2. In our method, random augmentation is omitted because the guidance is not computed by neural networks so the adversarial gradient issues are not obvious. The quantitative results of our investigation are summarized in Table 3, while Figure 6 showcases randomly selected samples. Our methods exhibit enhanced control quality over the generated motion. The videos are provided in the supplementary materials.

## 6 Conclusions

In this paper, we conducted a comprehensive investigation into training-free guidance, which employs pre-trained diffusion models and guides them using the off-the-shelf trained on clean images. Our exploration delved into the underlying mechanisms and fundamental limits of these models. Moreover, we proposed a set of enhancement techniques and verified their effectiveness both theoretically and empirically. **Limitations.** Despite our efforts to mitigate the shortcomings of training-free methods and enhance their performance, certain limitations remain. Notably, the refined training-free guidance still necessitates a higher number of NFEs when compared with extensive training methods such as classifier-free guidance. This is because adversarial gradient cannot be fully eliminated without training. **Ethical Consideration.** Similar to other models designed for image creation, our model also has the unfortunate potential to be used for creating deceitful or damaging material. We pledge to restrict the usage of our model exclusively to the realm of research to prevent such misuse.



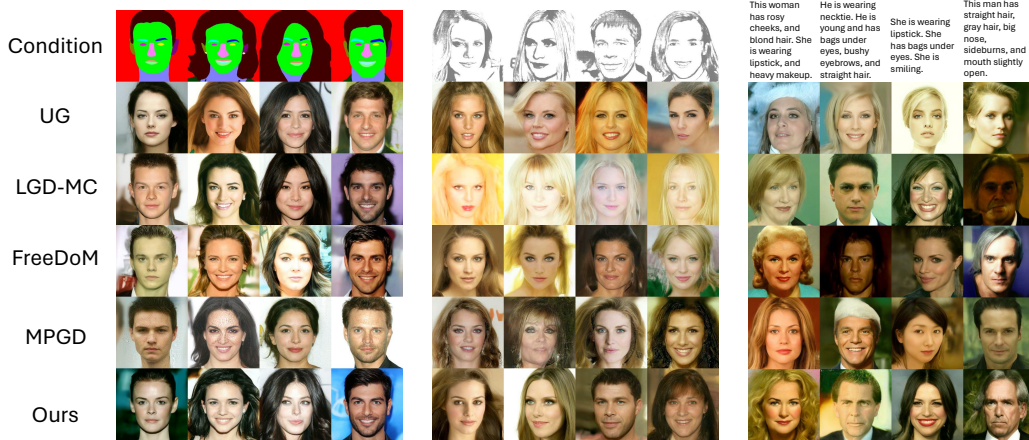


Figure 4: Qualitative results of CelebA-HQ with zero-shot segmentation, sketch, and text guidance. The images are randomly selected.



Figure 5: Qualitative results of ImageNet model with zero-shot text guidance. The images are randomly selected.

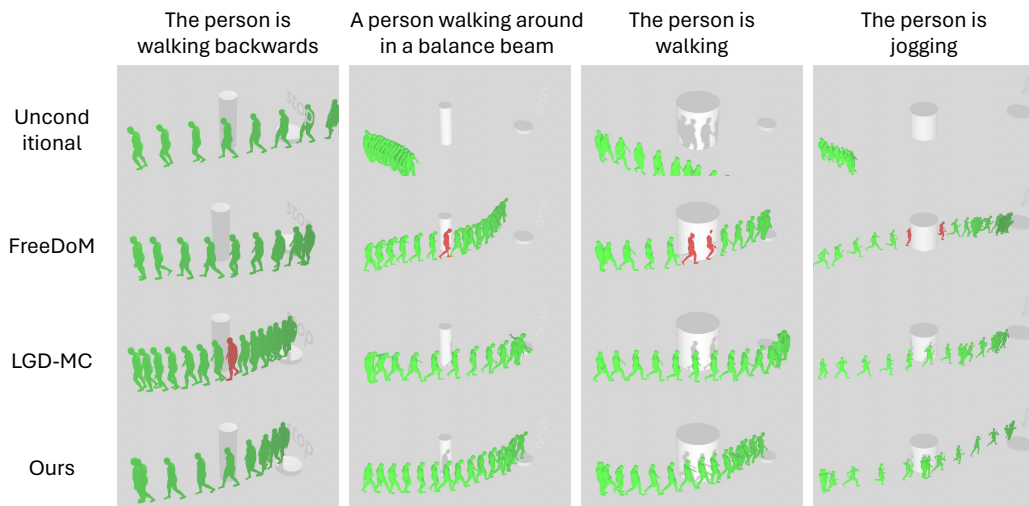


Figure 6: Qualitative results of human motion diffusion with zero-shot object avoidance and targeting guidance. Instances of intersection with obstacles are highlighted by marking the person in red. The trajectories are randomly selected.

## References

- [1] Anish Athalye, Logan Engstrom, Andrew Ilyas, and Kevin Kwok. Synthesizing robust adversarial examples. In *International conference on machine learning*, pp. 284–293. PMLR, 2018.
- [2] Arpit Bansal, Hong-Min Chu, Avi Schwarzschild, Soumyadip Sengupta, Micah Goldblum, Jonas Geiping, and Tom Goldstein. Universal guidance for diffusion models. In *Proceedings of the IEEE/CVF Conference on Computer Vision and Pattern Recognition*, pp. 843–852, 2023.
- [3] Tim Brooks, Bill Peebles, Connor Homes, Will DePue, Yufei Guo, Li Jing, David Schnurr, Joe Taylor, Troy Luhman, Eric Luhman, Clarence Ng, Ricky Wang, and Aditya Ramesh. Video generation models as world simulators. 2024. URL <https://openai.com/research/video-generation-models-as-world-simulators>.
- [4] Anirban Chakraborty, Manaar Alam, Vishal Dey, Anupam Chattopadhyay, and Debdeep Mukhopadhyay. Adversarial attacks and defences: A survey. *arXiv preprint arXiv:1810.00069*, 2018.
- [5] Yixuan Chen, Yubin Shi, Mingzhi Dong, Xiaochen Yang, Dongsheng Li, Yujiang Wang, Robert Dick, Qin Lv, Yingying Zhao, Fan Yang, et al. Over-parameterized model optimization with polyak-łojasiewicz condition. 2023.
- [6] Hyungjin Chung, Jeongsol Kim, Michael T Mccann, Marc L Klasky, and Jong Chul Ye. Diffusion posterior sampling for general noisy inverse problems. *arXiv preprint arXiv:2209.14687*, 2022.
- [7] Hyungjin Chung, Byeongsu Sim, Dohoon Ryu, and Jong Chul Ye. Improving diffusion models for inverse problems using manifold constraints. *Advances in Neural Information Processing Systems*, 35: 25683–25696, 2022.
- [8] Prafulla Dhariwal and Alexander Nichol. Diffusion models beat gans on image synthesis. *Advances in neural information processing systems*, 34:8780–8794, 2021.
- [9] Yinpeng Dong, Fangzhou Liao, Tianyu Pang, Hang Su, Jun Zhu, Xiaolin Hu, and Jianguo Li. Boosting adversarial attacks with momentum. In *Proceedings of the IEEE conference on computer vision and pattern recognition*, pp. 9185–9193, 2018.
- [10] Dave Epstein, Allan Jabri, Ben Poole, Alexei Efros, and Aleksander Holynski. Diffusion self-guidance for controllable image generation. *Advances in Neural Information Processing Systems*, 36, 2024.
- [11] Ian J Goodfellow, Jonathon Shlens, and Christian Szegedy. Explaining and harnessing adversarial examples. *arXiv preprint arXiv:1412.6572*, 2014.
- [12] Xu Han, Caihua Shan, Yifei Shen, Can Xu, Han Yang, Xiang Li, and Dongsheng Li. Training-free multi-objective diffusion model for 3d molecule generation. In *The Twelfth International Conference on Learning Representations*, 2023.
- [13] Elad Hazan and Sham Kakade. Revisiting the polyak step size. *arXiv preprint arXiv:1905.00313*, 2019.
- [14] Yutong He, Naoki Murata, Chieh-Hsin Lai, Yuhta Takida, Toshimitsu Uesaka, Dongjun Kim, Wei-Hsiang Liao, Yuki Mitsufuji, J Zico Kolter, Ruslan Salakhutdinov, et al. Manifold preserving guided diffusion. *arXiv preprint arXiv:2311.16424*, 2023.
- [15] Amir Hertz, Ron Mokady, Jay Tenenbaum, Kfir Aberman, Yael Pritch, and Daniel Cohen-Or. Prompt-to-prompt image editing with cross attention control. *arXiv preprint arXiv:2208.01626*, 2022.
- [16] Jonathan Ho and Tim Salimans. Classifier-free diffusion guidance. *arXiv preprint arXiv:2207.12598*, 2022.
- [17] Jonathan Ho, Ajay Jain, and Pieter Abbeel. Denoising diffusion probabilistic models. *Advances in neural information processing systems*, 33:6840–6851, 2020.
- [18] Emiel Hoogeboom, Victor Garcia Satorras, Clément Vignac, and Max Welling. Equivariant diffusion for molecule generation in 3d. In *International conference on machine learning*, pp. 8867–8887. PMLR, 2022.
- [19] Michael Janner, Yilun Du, Joshua Tenenbaum, and Sergey Levine. Planning with diffusion for flexible behavior synthesis. In *International Conference on Machine Learning*, pp. 9902–9915. PMLR, 2022.
- [20] Hamed Karimi, Julie Nutini, and Mark Schmidt. Linear convergence of gradient and proximal-gradient methods under the polyak-łojasiewicz condition. In *Machine Learning and Knowledge Discovery in Databases: European Conference, ECML PKDD 2016, Riva del Garda, Italy, September 19-23, 2016, Proceedings, Part I 16*, pp. 795–811. Springer, 2016.

- [21] Zhixuan Liang, Yao Mu, Mingyu Ding, Fei Ni, Masayoshi Tomizuka, and Ping Luo. Adaptdiffuser: Diffusion models as adaptive self-evolving planners. *arXiv preprint arXiv:2302.01877*, 2023.
- [22] Xihui Liu, Dong Huk Park, Samaneh Azadi, Gong Zhang, Arman Chopikyan, Yuxiao Hu, Humphrey Shi, Anna Rohrbach, and Trevor Darrell. More control for free! image synthesis with semantic diffusion guidance. In *Proceedings of the IEEE/CVF Winter Conference on Applications of Computer Vision*, pp. 289–299, 2023.
- [23] Xingchao Liu, Chengyue Gong, Lemeng Wu, Shujian Zhang, Hao Su, and Qiang Liu. Fusedream: Training-free text-to-image generation with improved clip+ gan space optimization. *arXiv preprint arXiv:2112.01573*, 2021.
- [24] Cheng Lu, Yuhao Zhou, Fan Bao, Jianfei Chen, Chongxuan Li, and Jun Zhu. Dpm-solver: A fast ode solver for diffusion probabilistic model sampling in around 10 steps. *Advances in Neural Information Processing Systems*, 35:5775–5787, 2022.
- [25] Cheng Lu, Huayu Chen, Jianfei Chen, Hang Su, Chongxuan Li, and Jun Zhu. Contrastive energy prediction for exact energy-guided diffusion sampling in offline reinforcement learning. *arXiv preprint arXiv:2304.12824*, 2023.
- [26] Andreas Lugmayr, Martin Danelljan, Andres Romero, Fisher Yu, Radu Timofte, and Luc Van Gool. Repaint: Inpainting using denoising diffusion probabilistic models. In *Proceedings of the IEEE/CVF Conference on Computer Vision and Pattern Recognition*, pp. 11461–11471, 2022.
- [27] Aleksander Madry, Aleksandar Makelov, Ludwig Schmidt, Dimitris Tsipras, and Adrian Vladu. Towards deep learning models resistant to adversarial attacks. *arXiv preprint arXiv:1706.06083*, 2017.
- [28] Koichi Miyasawa et al. An empirical bayes estimator of the mean of a normal population. *Bull. Inst. Internat. Statist.*, 38(181-188):1–2, 1961.
- [29] Sicheng Mo, Fangzhou Mu, Kuan Heng Lin, Yanli Liu, Bochen Guan, Yin Li, and Bolei Zhou. Freecontrol: Training-free spatial control of any text-to-image diffusion model with any condition. *arXiv preprint arXiv:2312.07536*, 2023.
- [30] Alec Radford, Jong Wook Kim, Chris Hallacy, Aditya Ramesh, Gabriel Goh, Sandhini Agarwal, Girish Sastry, Amanda Askell, Pamela Mishkin, Jack Clark, et al. Learning transferable visual models from natural language supervision. In *International conference on machine learning*, pp. 8748–8763. PMLR, 2021.
- [31] Robin Rombach, Andreas Blattmann, Dominik Lorenz, Patrick Esser, and Björn Ommer. High-resolution image synthesis with latent diffusion models. In *Proceedings of the IEEE/CVF conference on computer vision and pattern recognition*, pp. 10684–10695, 2022.
- [32] Hadi Salman, Jerry Li, Ilya Razenshteyn, Pengchuan Zhang, Huan Zhang, Sebastien Bubeck, and Greg Yang. Provably robust deep learning via adversarially trained smoothed classifiers. *Advances in Neural Information Processing Systems*, 32, 2019.
- [33] Hadi Salman, Andrew Ilyas, Logan Engstrom, Ashish Kapoor, and Aleksander Madry. Do adversarially robust imagenet models transfer better? *Advances in Neural Information Processing Systems*, 33:3533–3545, 2020.
- [34] Jiaming Song, Chenlin Meng, and Stefano Ermon. Denoising diffusion implicit models. *arXiv preprint arXiv:2010.02502*, 2020.
- [35] Jiaming Song, Qinsheng Zhang, Hongxu Yin, Morteza Mardani, Ming-Yu Liu, Jan Kautz, Yongxin Chen, and Arash Vahdat. Loss-guided diffusion models for plug-and-play controllable generation. 2023.
- [36] Christian Szegedy, Wojciech Zaremba, Ilya Sutskever, Joan Bruna, Dumitru Erhan, Ian Goodfellow, and Rob Fergus. Intriguing properties of neural networks. *arXiv preprint arXiv:1312.6199*, 2013.
- [37] Guy Tevet, Brian Gordon, Amir Hertz, Amit H Bermano, and Daniel Cohen-Or. Motionclip: Exposing human motion generation to clip space. In *European Conference on Computer Vision*, pp. 358–374. Springer, 2022.
- [38] Guy Tevet, Sigal Raab, Brian Gordon, Yonatan Shafir, Daniel Cohen-Or, and Amit H Bermano. Human motion diffusion model. *arXiv preprint arXiv:2209.14916*, 2022.
- [39] Shengbang Tong, Erik Jones, and Jacob Steinhardt. Mass-producing failures of multimodal systems with language models. *Advances in Neural Information Processing Systems*, 36, 2024.

- [40] Narek Tumanyan, Michal Geyer, Shai Bagon, and Tali Dekel. Plug-and-play diffusion features for text-driven image-to-image translation. In *Proceedings of the IEEE/CVF Conference on Computer Vision and Pattern Recognition*, pp. 1921–1930, 2023.
- [41] Roman Vershynin. *High-dimensional probability: An introduction with applications in data science*, volume 47. Cambridge university press, 2018.
- [42] Wei Wang, Dongqi Han, Xufang Luo, Yifei Shen, Charles Ling, Boyu Wang, and Dongsheng Li. Toward open-ended embodied tasks solving. In *NeurIPS 2023 Agent Learning in Open-Endedness Workshop*, 2023.
- [43] Xiaoyu Xiang, Ding Liu, Xiao Yang, Yiheng Zhu, Xiaohui Shen, and Jan P Allebach. Adversarial open domain adaptation for sketch-to-photo synthesis. In *Proceedings of the IEEE/CVF Winter Conference on Applications of Computer Vision*, 2022.
- [44] Yilun Xu, Mingyang Deng, Xiang Cheng, Yonglong Tian, Ziming Liu, and Tommi Jaakkola. Restart sampling for improving generative processes. *Advances in Neural Information Processing Systems*, 36, 2024.
- [45] Changqian Yu, Jingbo Wang, Chao Peng, Changxin Gao, Gang Yu, and Nong Sang. Bisenet: Bilateral segmentation network for real-time semantic segmentation. In *Proceedings of the European conference on computer vision (ECCV)*, pp. 325–341, 2018.
- [46] Jiwen Yu, Yinhuai Wang, Chen Zhao, Bernard Ghanem, and Jian Zhang. Freedom: Training-free energy-guided conditional diffusion model. *arXiv preprint arXiv:2303.09833*, 2023.
- [47] Lvmin Zhang, Anyi Rao, and Maneesh Agrawala. Adding conditional control to text-to-image diffusion models. In *Proceedings of the IEEE/CVF International Conference on Computer Vision*, pp. 3836–3847, 2023.
- [48] Shengyu Zhao, Zhijian Liu, Ji Lin, Jun-Yan Zhu, and Song Han. Differentiable augmentation for data-efficient gan training. *Advances in neural information processing systems*, 33:7559–7570, 2020.
- [49] Shuxin Zheng, Jiyan He, Chang Liu, Yu Shi, Ziheng Lu, Weitao Feng, Fusong Ju, Jiayi Wang, Jianwei Zhu, Yaosen Min, et al. Towards predicting equilibrium distributions for molecular systems with deep learning. *arXiv preprint arXiv:2306.05445*, 2023.

## A Related Works

### A.1 Training-Free Control for Diffusion

The current training-free control strategies for diffusion models can be divided into two primary categories. The first category is the investigated topic in this paper, which is universally applicable to universal control formats and diffusion models. These methods predict a clean image, subsequently leveraging pre-trained networks to guide the diffusion process. Central to this approach are the algorithms based on (5), which have been augmented through techniques like time-travel [2, 46] and the introduction of Gaussian noise [35]. Extensions of these algorithms have found utility in domains with constrained data-condition pairs, such as molecule generation [12], and in scenarios necessitating zero-shot guidance, like open-ended goals in offline reinforcement learning [42]. In molecular generation and offline reinforcement learning, they outperform training-based alternatives as additional training presents challenges. This paper delves deeper into the mechanics of this paradigm and introduces a suite of enhancements to bolster its performance. The efficacy of our proposed modifications is demonstrated across image and motion generation, with promising potential for generalization to molecular modeling and reinforcement learning tasks.

The second category of training-free control is tailored to text-to-image or text-to-video diffusion models, which is based on insights into their internal backbone architecture. For instance, object layout and shape have been linked to the cross-attention mechanisms [15], while network activations have been shown to preserve object appearance [40]. These understandings facilitate targeted editing of object layout and appearance (Diffusion Self-Guidance [10]) and enable the imposition of conditions in ControlNet through training-free means (FreeControl [29]). Analyzing these methodologies is challenging due to their reliance on emergent representations during training. Nonetheless, certain principles from this paper remain relevant; for example, as noted in Proposition 3.3, these methods often necessitate extensive diffusion steps, with instances such as [29, 10] employing 1000 steps. A thorough examination and refinement of these techniques remain an avenue for future research.

### A.2 Training-based Gradient Guidance

The training-based gradient guidance paradigm, such as classifier guidance, is a predominant approach for diffusion guidance. The core objective is to train a time-dependent network that approximates  $p_t(\mathbf{y}|\mathbf{x}_t)$  in the RHS of (2), and to utilize the resulting gradient as guidance. The most well-known example is classifier guidance, which involves training a classifier on noisy images. However, classifier guidance is limited to class conditions and is not adaptable to other forms of control, such as image and text guidance. To address this limitation, there are two main paradigms. The first involves training a time-dependent network that aligns features extracted from both clean and noisy images, as described by [22]. The training process is outlined as follows:

$$\min_{\psi} \mathbb{E}_{p(\mathbf{x}_0, \mathbf{x}_t)} d(f_{\psi}(\mathbf{x}_t, t), f_{\phi}(\mathbf{x}_0)),$$

where  $d(\cdot, \cdot)$  represents a loss function, such as cross-entropy or the  $\ell_2$  norm. If time-dependent networks for clean images are already available, training can proceed in a self-supervised fashion without the need for labeled data. The second paradigm, as outlined by [19], involves training an energy-based model to approximate  $p_t(\mathbf{y}|\mathbf{x}_t)$ . The training process is described as follows:

$$\min_{\psi} \mathbb{E}_{p(\mathbf{x}_0, \mathbf{x}_t)} |\ell(f_{\psi}(\mathbf{x}_t, t), \mathbf{y}) - \ell(f_{\phi}(\mathbf{x}_0), \mathbf{y})|.$$

However, it is observed in [25] that none of these methods can accurately approximate the true energy in (4). The authors of [25] propose an algorithm to learn the true energy. The loss function is a contrastive loss

$$\min_{\psi} \mathbb{E}_{p(\mathbf{x}_0^i, \mathbf{x}_t^i)} \exp(-\ell(f_{\phi}(\mathbf{x}_0), \mathbf{y})) \left[ -\sum_{i=1}^K \log \frac{\exp(\ell(f_{\psi}(\mathbf{x}_t^i, t), \mathbf{y}^i))}{\sum_{j=1}^K \exp(-\ell(f_{\psi}(\mathbf{x}_t^j, t), \mathbf{y}^j))} \right],$$

where  $(\mathbf{x}_0^i, \mathbf{x}_t^i)$  are  $K$  paired data samples from  $p(\mathbf{x}_0^i, \mathbf{y}^i)$ . Theorem 3.2 in [25] proves that the optimal  $f_{\psi^*}$  satisfied that  $\nabla_{\mathbf{x}_t} \ell(f_{\psi^*}(\mathbf{x}_t^i, t), \mathbf{y}^i) = \nabla_{\mathbf{x}_t} p_t(\mathbf{y}|\mathbf{x}_t)$ .

**Although this paper focuses on training-free guidance, the findings in this paper can be naturally extended to all training-based gradient guidance schemes.** Firstly, the issue of adversarial gradients

cannot be resolved without additional training; hence, all the aforementioned methods are subject to adversarial gradients. Empirical evidence for this is presented in Fig. 2, which illustrates that the gradients from an adversarially robust classifier are markedly more vivid than those from time-dependent classifiers. Consequently, it is anticipated that incorporating additional adversarial training into these methods would enhance the quality of the generated samples. Secondly, since these methods are dependent on gradients, employing a more sophisticated gradient solver could further improve their NFEs.

### A.3 Adversarial Attack and Robustness

Adversarial attacks and robustness constitute a fundamental topic in deep learning [4]. An adversarial attack introduces minimal, yet strategically calculated, changes to the original data that are often imperceptible to humans, leading models to make incorrect predictions. The most common attacks are gradient-based, for example, the Fast Gradient Sign Method (FGSM) [11], Projected Gradient Descent (PGD) [27], Smoothed Gradient Attacks [1], and Momentum-Based Attacks [9]. An attack is akin to classifier guidance or training-free guidance, which uses the gradient of a pre-trained network for guidance. Should the gradient be adversarial, the guidance will be compromised. This paper establishes the relationship between training-free loss-guided diffusion models and adversarial attacks in two ways. Firstly, we prove that training-free guidance is more sensitive to an adversarial gradient. Secondly, in Section 4.2, we demonstrate that borrowing an adaptive gradient scheduler can improve convergence. The optimizers from adversarial attack literature may also expedite the convergence of the diffusion ODE.

## B Baselines and Experimental Settings

### B.1 Details of the Baselines

We use the following training-free diffusion guidance methods as baselines for comparison:

- **Universal Guidance (UG)** [2] employs guidance as delineated in (5) and uses time-travel strategies outlined in Algorithm 3 to enhance performance. The time-travel trick is used for all time steps  $t$ .
- **FreeDoM** [46] is also founded on (5) and time-travel trick. In addition, FreeDoM incorporates a time-dependent step size for each gradient guidance and judiciously selects the diffusion step for executing time-travel trick.
- **Loss-guided Diffusion with Monte Carlo (LGD-MC)** [35] utilizes guidance from (6) and we set  $n = 10$  in the experiments.
- **Manifold Guided Preserving Diffusion (MPGD)** [14] takes the derivative with respect to estimated clean image  $\mathbb{E}[\mathbf{x}_0|\mathbf{x}_t]$  instead of  $\mathbf{x}_t$ . Let  $\mathbf{x}_{0|t} = \mathbb{E}[\mathbf{x}_0|\mathbf{x}_t]$ , MPGD steps are expressed as following:

$$\nabla_{\mathbf{x}_t} \log p_t(\mathbf{y}|\mathbf{x}_t) := -\sqrt{\alpha_{t-1}} \nabla_{\mathbf{x}_{0|t}} \log [\exp(-\ell(f_\phi(\mathbf{x}_{0|t}), \mathbf{y}))].$$

MPGD-Z adopts an additional auto-encoder to preserve manifold constraints. The details procedures of MPGD-Z are described in Algorithm 3 of [14].

### B.2 MPGD for Motion Diffusion

For the process of motion diffusion, the application of both MPGD-Z and MPGD-AE is precluded due to the absence of pretrained auto-encoders specific to motion diffusion. An implementation of MPGD without projection (MPGD w/o proj) was attempted for motion diffusion; however, it was unsuccessful in accurately navigating towards the target. This failure is attributed to the presence of spurious correlations within the targeting loss specific to MPGD, a phenomenon not observed in the other baseline methodologies. Specially, the gradient formulation in MPGD is detailed as follows:

$$\text{grad\_MPGD} = \begin{cases} 2(\mathbf{y}_{\text{target}} - \mathbf{x}_{0|t}) & \text{if } t == T \\ 0 & \text{otherwise} \end{cases}$$

The gradient in FreeDoM and other methods is given by

$$\text{grad\_DPS} = 2(\mathbf{y}_{\text{target}} - \mathbf{x}_{0|t}) \cdot \frac{\mathbf{I} + \sigma_t^2 \nabla^2 \log p_t(\mathbf{x}_t)}{\sqrt{\alpha_t}}.$$

Analysis of the aforementioned equations reveals that, within the MPGD framework, only the final motion step is influenced by the gradient, a characteristic not shared by alternative methodologies. Consequently, this exclusive focus on the last step results in disproportionately strong guidance at this juncture, while earlier steps suffer from a lack of directional input. This imbalance may adversely affect the overall quality of the samples produced. Empirical observations substantiate that MPGD struggles to achieve targeted outcomes when a nuanced adjustment of step size is required. Given these limitations, MPGD has been excluded from the comparative analysis presented in Table 3.

### B.3 Prompts for Motion Diffusion

We follow the prompts and evaluation settings in [35]. The prompts are (i) “the person is walking backwards”; (ii) “a person walking around in a balance beam”; (iii) “the person is walking”; (iv) “the person is jogging”. We consider three different directions for each prompt, and each direction has 10 random seeds, the metrics are then averaged together over the 30 synthesized motions.

## C More Discussions

### C.1 Concentration of Estimated Clean Samples

It has been demonstrated in [7] that, given a fixed  $\mathbf{x}_0$ , the distribution of the noisy data  $\mathbf{x}_t$  is concentrated on a spherical shell. Furthermore, an extension of this theorem presented in the ‘High Dimensional Probability’ textbook by Vershynin [41] elucidates that the conditional distribution  $q(\mathbf{x}_0|\mathbf{x}_t)$  also exhibits concentration on a spherical shell, provided that its coordinates are sub-Gaussian.

**Theorem C.1.** (Theorem 3.1.1 in [41]) Denote  $\mathbf{x}_0 = \mathbf{x}_t + \mathbf{g} \in \mathbb{R}^n$ , where  $\mathbf{g} = (g_1, \dots, g_n)$ . Assume that  $g_i$  are independent identically distributed,  $\mathbb{E}[g_i^2] = \frac{r_t^2}{n}$  and there exists constant  $c_1$  such that  $\mathbb{P}[g_i \geq t] \leq \exp(-c_1 t^2)$ , then we have

$$\mathbb{P}[|\|\mathbf{x}_t - \mathbf{x}_0\|_2^2 - r_t^2| \geq t] \leq \exp(-c_2 n t^2),$$

where  $c_2$  is a constant.

Theorem C.1 establishes that the distribution  $q(\mathbf{x}_0|\mathbf{x}_t)$  exhibits concentration on a spherical shell at an exponential rate. For high-dimensional data, such as images, it is reasonable to infer that  $\mathbf{x}_0$  is predominantly situated on this spherical shell.

### C.2 Time-travel Trick

---

#### Algorithm 3 Time Travel

---

```

1: for  $t = T, \dots, 1$  do
2:   for  $i = 1, \dots, s$  do
3:      $\mathbf{x}_{t-1}^i = \text{DDIM with Guidance}(\mathbf{x}_t^{i-1})$ 
4:     if  $i < s$  then
5:        $\beta_t = \alpha_t / \alpha_{t-1}$ ,  $\mathbf{n} \sim \mathcal{N}(0, \mathbf{I})$ 
6:        $\mathbf{x}_t^i = \sqrt{\beta_t} \mathbf{x}_{t-1}^i + \sqrt{1 - \beta_t} \mathbf{n}$ 
7:     end if
8:      $\mathbf{x}_{t-1}^0 = \mathbf{x}_{t-1}^s$ 
9:   end for
10: end for

```

---

The technique of time-travel, also referred to as “resampling”, has been proposed as a solution to complex generative problems [26], facilitating successful training-free guidance in tasks such as

CLIP-guided ImageNet generation and layout guidance for stable diffusion, as illustrated in Figure 2 of [46] and Figure 8 of [2], respectively. The procedure of the time-travel trick is shown in Algorithm 3, which involves recursive execution of individual sampling steps.

In this subsection, we endeavor to analyze the role of time-travel trick in training-free guidance and thus complete the overall picture. During the diffusion process, samples can diverge from their target distributions due to various types of sampling error, such as adversarial gradient and discretization error. A critical component of the time-travel trick process entails the reintroduction of random noise to transition the sample  $\mathbf{x}_{t-1}$  back to  $\mathbf{x}_t$ , effectively resetting the sampling state. The forthcoming lemma substantiates the premise that the act of adding identical noise to two vectors serves to diminish the disparity between the samples.

**Lemma C.2.** (Adding noise removes the discrepancy; Lemma 7 of [44]) Suppose  $\mathbf{n}_x, \mathbf{n}_y \sim \mathcal{N}(0, \sigma^2 \mathbf{I})$ , and  $\mathbf{x}' = \mathbf{x} + \mathbf{n}_x, \mathbf{y}' = \mathbf{y} + \mathbf{n}_y$ . Then we have  $TV(\mathbf{x}', \mathbf{y}') = 1 - 2Q(r)$ , where  $Q(\cdot)$  is Gaussian tail probability defined in Definition D.3 in appendix and  $r = \|\mathbf{x} - \mathbf{y}\|/(2\sigma)$ .

Following Lemma C.2, the next proposition demonstrates that the total variation distance between the sampled distribution  $q_t(\mathbf{x}_t^i)$ , as obtained in the  $i$ -th time travel of Algorithm 3, and the ground-truth distribution  $p_t(\mathbf{x}_t)$ , is progressively reduced through recursive application of the time-travel steps.

**Proposition C.3.** Denote  $p_t(\mathbf{x}_t)$  and  $q_t(\mathbf{x}_t)$  as the ground-truth distribution and the distribution sampled by Algorithm 3, and  $2\|\mathbf{x}_t\| \leq B$ . Then we have

$$TV(q_t(\mathbf{x}_t^s), p_t(\mathbf{x}_t)) \leq \left(1 - 2Q\left(\frac{\sqrt{\beta_t}B}{2\sqrt{1-\beta_t}}\right)\right)^{s-1} TV(q_t(\mathbf{x}_t^1), p_t(\mathbf{x}_t)) + O(h_{\max}),$$

where  $h_{\max}$  is defined in Proposition 3.3.

The proof is presented in Appendix D.6. Proposition C.3 indicates that the time-travel technique serves to “rectify” the distributional divergence caused by guidance. This aspect is crucial, as we have demonstrated that training-free guidance is particularly susceptible to adversarial gradients, which steer the images away from the natural image distribution. The time-travel technique realigns these images with the distribution of natural images.

### C.3 Efficiency of Random Augmentation

Given the multiple invocations of the guidance network necessitated by random augmentation (RA), concerns regarding the efficiency of this approach are understandable. However, it is important to note that, compared to the diffusion backbone, the guidance network exhibits a more lightweight architecture, thereby mitigating any significant increase in computational demand. To empirically illustrate this point, we present the computation times associated with varying degrees of augmentation in Table 4. In the conducted experiments, we set the cardinality of the set  $\mathcal{T}$  to 10, thereby having little impact on the inference time. These experiments were conducted on a single NVIDIA A100 GPU.

Setting	w/o RA	$ \mathcal{T}  = 1$	$ \mathcal{T}  = 10$	$ \mathcal{T}  = 20$	$ \mathcal{T}  = 30$
CLIP Score	0.541	0.544	0.571	0.592	0.625

Table 4: Inference time (seconds per diffusion step) of different random augmentation configurations. The diffusion backbone is ImageNet diffusion and the guidance network is CLIP-B/16.

## D Proofs

### D.1 Definitions

This subsection introduces a few definitions that are useful in the following sections.

**Definition D.1.** ( $L$ -Lipschitz) A function  $f : \mathbb{R}^n \rightarrow \mathbb{R}^m$  is said to be  $L$ -Lipschitz if there exists a constant  $L \geq 0$  such that  $\|f(\mathbf{x}_2) - f(\mathbf{x}_1)\| \leq L\|\mathbf{x}_2 - \mathbf{x}_1\|$  for all  $\mathbf{x}_1, \mathbf{x}_2 \in \mathbb{R}^n$ .

**Definition D.2.** (PL condition) A function  $f : \mathbb{R}^n \rightarrow \mathbb{R}$  satisfies PL condition with parameter  $\mu$  if  $\|\nabla f(\mathbf{x})\|^2 \geq \mu f(\mathbf{x})$ .

**Definition D.3.** (Q function) We define the Gaussian tail probability  $Q(x) = \mathbb{P}(x \geq a), x \sim \mathcal{N}(0, 1)$ .



## D.2 Proof for Proposition 3.1

Denote  $\hat{\mathbf{x}}_0 = \mathbb{E}_{p(\mathbf{x}_0|\mathbf{x}_t)}(\mathbf{x}_0)$ , the gradient guidance term in (5) can be written as the following:

$$\nabla_{\mathbf{x}_t} \ell[f_\phi(\hat{\mathbf{x}}_0), \mathbf{y}] = \frac{\partial \ell}{\partial \hat{\mathbf{x}}_0} \nabla_{\mathbf{x}_t} \left( \frac{\mathbf{x}_t + \sigma_t^2 \nabla_{\mathbf{x}_t} \log p_t(\mathbf{x}_t)}{\sqrt{\alpha_t}} \right) = \frac{\partial \ell}{\partial \hat{\mathbf{x}}_0} \frac{\text{Cov}[\mathbf{x}_0|\mathbf{x}_t]}{\sigma_t^2 \sqrt{\alpha_t}}, \quad (9)$$

where the last equality follows the second-order Miyasawa relationship  $\text{Cov}[\mathbf{x}_0|\mathbf{x}_t] = \sigma_t^2(\mathbf{I} + \sigma_t^2 \nabla^2 \log p_t(\mathbf{x}_t))$  [28].

For the first condition, the Lipschitz constant satisfies

$$\begin{aligned} |\ell_t(\mathbf{x}_1) - \ell_t(\mathbf{x}_2)| &\leq \frac{L_f}{\sqrt{\alpha_t}} |\mathbf{x}_1 - \nabla_{\mathbf{x}_1} \log p_t(\mathbf{x}_1) - \mathbf{x}_2 + \nabla_{\mathbf{x}_2} \log p_t(\mathbf{x}_2)| \\ &\leq L_f(1 + L_p) \|\mathbf{x}_1 - \mathbf{x}_2\|, \end{aligned}$$

and the PL constant satisfies

$$\ell_t(\mathbf{x}_t) \leq \frac{1}{\mu} \left\| \frac{\partial \ell}{\partial \hat{\mathbf{x}}_0} \right\|^2 = \frac{1}{\mu} \|\nabla_{\mathbf{x}_t} \ell \cdot \text{Cov}^{-1}(\mathbf{x}_0|\mathbf{x}_t) \sigma_t^2 \sqrt{\alpha_t}\|^2 \leq \frac{\sigma_t^4 \alpha_t}{\mu \lambda_{\min}^2} \|\nabla_{\mathbf{x}_t} \ell\|^2.$$

The second and third conditions directly follow Lemma D.4.

**Lemma D.4.** (Linear Convergence Under PL condition; [20]) Denote  $\mathbf{x}^0$  as the initial point and  $\mathbf{x}^t$  as the point after  $t$  gradient steps. If the function is  $L$ -Lipschitz and  $\mu$ -PL, gradient descent with a step size  $\eta = \frac{1}{L}$  converges to a global solution with  $\ell(\mathbf{x}^t) \leq (1 - \mu/L)^t \ell(\mathbf{x}^0)$ .

## D.3 Proof for Proposition 3.2

*Proof.* The proof of this theorem is based on the proof of Lemma 1 in [32]. By the definition of expectation, we have

$$\begin{aligned} \hat{f}(\mathbf{x}) &= \mathbb{E}_{\epsilon \sim \mathcal{N}(0, \mathbf{I})}[f(\mathbf{x} + \sigma_t \epsilon)] = (f \otimes \mathcal{N}(0, \sigma_t^2 \mathbf{I}))(\mathbf{x}) \\ &= \frac{1}{(2\pi\sigma_t^2)^{n/2}} \int_{\mathbb{R}^n} f(\mathbf{z}) \exp\left(-\frac{1}{2\sigma_t^2} \|\mathbf{x} - \mathbf{z}\|^2\right) d\mathbf{z}. \end{aligned}$$

We then show that for any unit direction  $\mathbf{u}$ ,  $\mathbf{u}^T \nabla \hat{f}(\mathbf{x}) \leq \sqrt{\frac{2}{\pi\sigma_t^2}}$ . The derivative of  $\hat{f}$  is given by

$$\begin{aligned} \nabla \hat{f}(\mathbf{x}) &= \frac{1}{(2\pi\sigma_t^2)^{n/2}} \int_{\mathbb{R}^n} f(\mathbf{z}) \nabla \exp\left(-\frac{1}{2\sigma_t^2} \|\mathbf{x} - \mathbf{z}\|^2\right) d\mathbf{z} \\ &= \frac{1}{(2\pi\sigma_t^2)^{n/2} \sigma_t^2} \int_{\mathbb{R}^n} f(\mathbf{z}) (\mathbf{x} - \mathbf{z}) \exp\left(-\frac{1}{2\sigma_t^2} \|\mathbf{x} - \mathbf{z}\|^2\right) d\mathbf{z}. \end{aligned}$$

Thus, the Lipschitz constant is computed as

$$\begin{aligned} \mathbf{u}^T \nabla \hat{f}(\mathbf{x}) &\leq \frac{C}{(2\pi\sigma_t^2)^{n/2}} \int_{\mathbb{R}^n} |\mathbf{u}^T (\mathbf{x} - \mathbf{z}) / \sigma_t^2| \exp\left(-\frac{1}{2\sigma_t^2} \|\mathbf{x} - \mathbf{z}\|^2\right) d\mathbf{z} \\ &= \frac{C}{(2\pi\sigma_t^2)^{1/2}} \int_{-\infty}^{\infty} |s| \exp\left(-\frac{1}{2}s^2\right) ds = \sqrt{\frac{2}{\pi\sigma_t^2}}. \end{aligned}$$

Similarly, for the Lipschitz constant of the gradient, we have

$$\begin{aligned} \|\nabla^2 \hat{f}(\mathbf{x})\|_{\text{op}} &\leq \|\nabla^2 \hat{f}(\mathbf{x})\|_2 \\ &\leq \frac{C}{\sqrt{2\pi}\sigma_t \cdot \sigma_t^4} \left( \int_{-\infty}^{\infty} s^2 \exp(-\frac{1}{2}s^2/\sigma_t^2) ds + \int_{-\infty}^{\infty} \sigma_t^2 \exp(-\frac{1}{2}s^2/\sigma_t^2) ds \right) = \frac{2C}{\sigma_t}. \end{aligned}$$

□

#### D.4 Proof for Proposition 3.3

*Proof.* We first analyze the discretization error of a single step from time  $s$  to  $t$ . We denote the update variable for DDIM is  $\mathbf{x}_t^*$  and the optimal solution of the diffusion ODE at time  $t$  as  $\mathbf{x}_t^*$ . Let  $\sigma_t = \sqrt{1 - \alpha_t}$ ,  $\lambda_t = \frac{1}{2} \log(\frac{\alpha_t}{1 - \alpha_t})$  and  $h = \lambda_t - \lambda_s$ . According to (B.4) of [24], the update of DDIM solver is given by

$$\mathbf{x}_t = \sqrt{\frac{\alpha_t}{\alpha_s}} \mathbf{x}_s - \sigma_t(e^h - 1) \epsilon_\theta(\mathbf{x}_s, s).$$

A similar relationship can be obtained for the optimal solution

$$\mathbf{x}_t^* = \sqrt{\frac{\alpha_t}{\alpha_s}} \mathbf{x}_s^* - \sigma_t(e^h - 1) \epsilon_\theta(\mathbf{x}_s^*, s) + O(h^2).$$

We then bound the error between  $\mathbf{x}_t$  and  $\mathbf{x}_t^*$ . We have

$$\begin{aligned} \mathbf{x}_t &\leq \sqrt{\frac{\alpha_t}{\alpha_s}} \mathbf{x}_s - \sigma_t(e^h - 1) (\epsilon_\theta(\mathbf{x}_s^*, s) + L(\mathbf{x}_s - \mathbf{x}_s^*)) \\ &= \sqrt{\frac{\alpha_t}{\alpha_s}} \mathbf{x}_s^* - \sigma_t(e^h - 1) \epsilon_\theta(\mathbf{x}_s^*, s) + \sqrt{\frac{\alpha_t}{\alpha_s}} (\mathbf{x}_t - \mathbf{x}_s^*) - \sigma_t(e^h - 1) L(\mathbf{x}_s - \mathbf{x}_s^*) \\ &= \mathbf{x}_t^* + O(h^2) + O(Lh^2). \end{aligned}$$

If we run DDIM for  $M$  steps,  $h_{\max} = O(1/M)$ , and we achieve the discretization error bound for DDIM algorithm:

$$\mathbf{x}_0 = \mathbf{x}_0^* + O(M(h_{\max}^2 + h_{\max}^2 L)) = \mathbf{x}_0^* + O(h_{\max} + h_{\max} L).$$

□

#### D.5 Proof for Proposition 4.1

*Proof.* By the definition of expectation, we have

$$\hat{f}(\mathbf{x}) = \mathbb{E}_{\epsilon \sim p(\epsilon)} [f(\mathbf{x} + \sigma_t \epsilon)] = (f \circledast p)(\mathbf{x}) = \int_{\mathbb{R}^n} f(\mathbf{z}) p(\mathbf{x} - \mathbf{z}) d\mathbf{z}.$$

Then we compute the Lipschitz constant

$$\mathbf{u}^T \nabla \hat{f}(\mathbf{x}) \leq C \int_{\mathbb{R}^n} \|\nabla p(\mathbf{x} - \mathbf{z})\|_2 d\mathbf{z} = C \int_{\mathbb{R}^n} \|\nabla p(\mathbf{z})\|_2 d\mathbf{z}.$$

As for the gradient Lipschitz constant, we have

$$L = \|\nabla^2 \hat{f}(\mathbf{x})\|_{\text{op}} \leq C \left\| \int_{\mathbb{R}^n} \nabla^2 p(\mathbf{x} - \mathbf{z}) d\mathbf{z} \right\|_{\text{op}} \leq C \int_{\mathbb{R}^n} \|\nabla^2 p(\mathbf{z})\|_{\text{op}} d\mathbf{z},$$

where  $\|\cdot\|_{\text{op}}$  is the operator norm of a matrix. □

#### D.6 Proof for Proposition C.3

Our proof is based on the proof for Theorem 2 in [44]. The total error can be decomposed as the discrepancy between  $q(\mathbf{x}_t^1)$  and  $p_t(\mathbf{x}_t)$  and the error introduced by the ODE solver. We introduce an auxiliary process  $q_t^r(\mathbf{y}_t^i)$ , which initiates from the true distribution and perform the time-travel steps. By triangle inequality:

$$\text{TV}(q_t(\mathbf{x}_t^i), p_t(\mathbf{x}_t)) \leq \text{TV}(q_t(\mathbf{x}_t^i), q_t^r(\mathbf{y}_t^i)) + \text{TV}(q_t^r(\mathbf{y}_t^i), p_t(\mathbf{x}_t)),$$

where the second term of RHS is bounded by  $O(h_{\max})$  according to Proposition 3.3. Then we follow Lemma 1 in [44] to bound the first term.

$$\begin{aligned} &\mathbb{E}[\mathbf{1}[\mathbf{x}_t^{i+1} \neq \mathbf{y}_t^{i+1}]] \leq \mathbb{E}[\mathbf{1}[\mathbf{x}_{t+1}^{i+1} \neq \mathbf{y}_{t+1}^{i+1}]] \\ &\stackrel{(a)}{\leq} \mathbb{E} \left[ \left( 1 - Q \left( \frac{\sqrt{\beta_t} B}{2\sqrt{1 - \beta_t}} \right) \right) \mathbf{1}[\mathbf{x}_t^i \neq \mathbf{y}_t^i] \right] \\ &= \left( 1 - Q \left( \frac{\sqrt{\beta_t} B}{2\sqrt{1 - \beta_t}} \right) \right) \mathbb{E}[\mathbf{1}[\mathbf{x}_t^i \neq \mathbf{y}_t^i]], \end{aligned}$$

where (a) uses Lemma C.2 by setting  $\mathbf{x}_{t+1}^{i+1} = \sqrt{\beta_t} \mathbf{x}_t^i + \sqrt{1 - \beta_t} \mathbf{n}$  and  $\mathbf{y}_{t+1}^{i+1} = \sqrt{\beta_t} \mathbf{y}_t^i + \sqrt{1 - \beta_t} \mathbf{n}$ . Applying the bound recursively, we have

$$\mathbb{E}[\mathbf{1}[\mathbf{x}_t^s \neq \mathbf{y}_t^s]] \leq \left(1 - Q\left(\frac{\sqrt{\beta_t} B}{2\sqrt{1 - \beta_t}}\right)\right)^{s-1} \mathbb{E}[\mathbf{1}[\mathbf{x}_t^1 \neq \mathbf{y}_t^1]].$$

The conclusion follows by  $\text{TV}(q_t(\mathbf{x}_t^i), q_t^r(\mathbf{y}_t^i)) \leq \mathbb{P}(\mathbf{x}_t^s \neq \mathbf{y}_t^s) = \mathbb{E}(\mathbf{1}[\mathbf{x}_t^s \neq \mathbf{y}_t^s])$  and the initial coupling  $\text{TV}(q_t(\mathbf{x}_t^1), q_t^r(\mathbf{y}_t^1)) = \mathbb{P}(\mathbf{x}_t^1 \neq \mathbf{y}_t^1)$ . Therefore, we conclude that

$$\begin{aligned} \text{TV}(q_t(\mathbf{x}_t^i), p_t(\mathbf{x}_t)) &\leq \text{TV}(q_t(\mathbf{x}_t^i), q_t^r(\mathbf{y}_t^i)) + \text{TV}(q_t^r(\mathbf{y}_t^i), p_t(\mathbf{x}_t)) \\ &\leq \left(1 - Q\left(\frac{\sqrt{\beta_t} B}{2\sqrt{1 - \beta_t}}\right)\right)^{s-1} \text{TV}(q_t(\mathbf{x}_t^1), q_t^r(\mathbf{y}_t^1)) + O(h_{\max}) \\ &\leq \left(1 - Q\left(\frac{\sqrt{\beta_t} B}{2\sqrt{1 - \beta_t}}\right)\right)^{s-1} \text{TV}(q_t(\mathbf{x}_t^1), p_t(\mathbf{x}_t)) + O(h_{\max}) + O(h_{\max}). \end{aligned}$$

## E More Qualitative Results

### E.1 CelebA-HQ



Figure 7: More qualitative results of CelebA-HQ with zero-shot segmentation guidance. The images are randomly selected.

### E.2 ImageNet



Figure 8: More qualitative results of CelebA-HQ with zero-shot sketch guidance. The images are randomly selected.

### E.3 Human Motion

See “TeX Source/videos.pptx”.

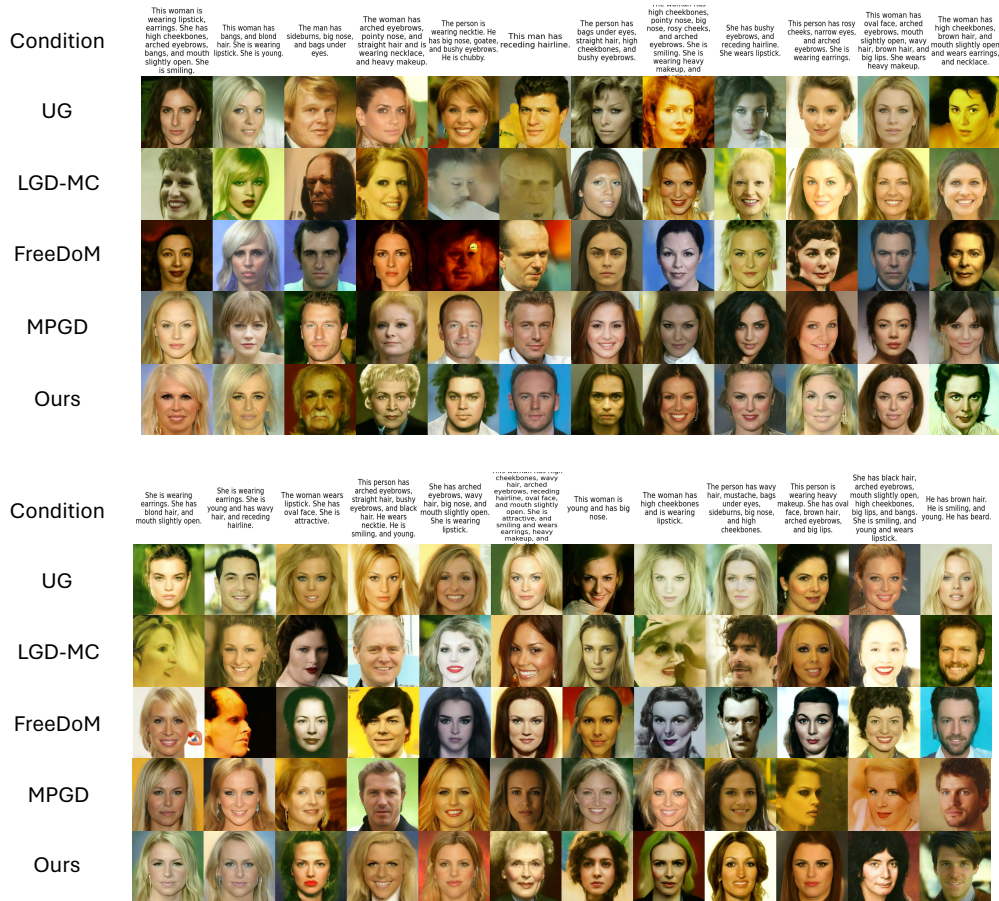


Figure 9: More qualitative results of CelebA-HQ with zero-shot text guidance. The images are randomly selected.

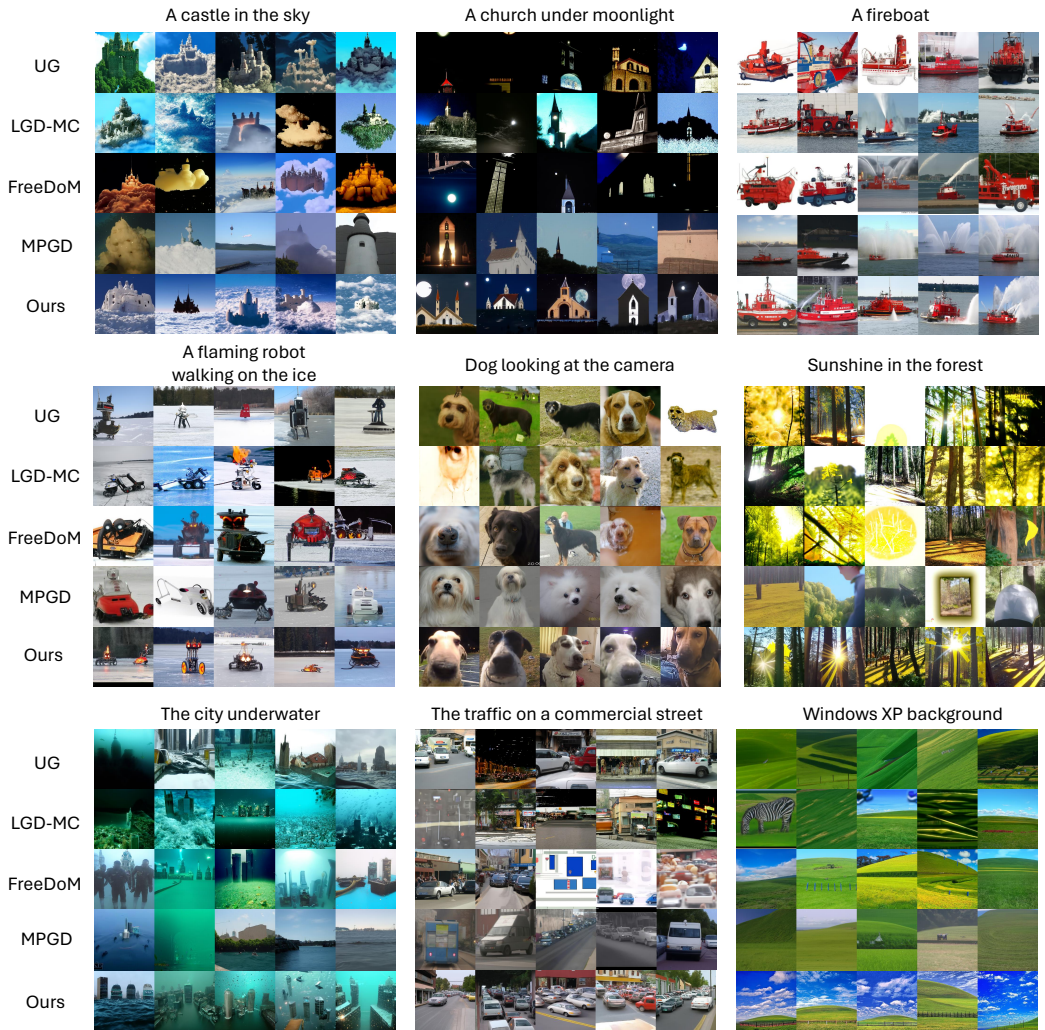


Figure 10: More qualitative results of ImageNet with zero-shot text guidance. The images are randomly selected.